ISTFA™ 2020

Papers Planned for the 46th International Symposium for Testing and Failure Analysis

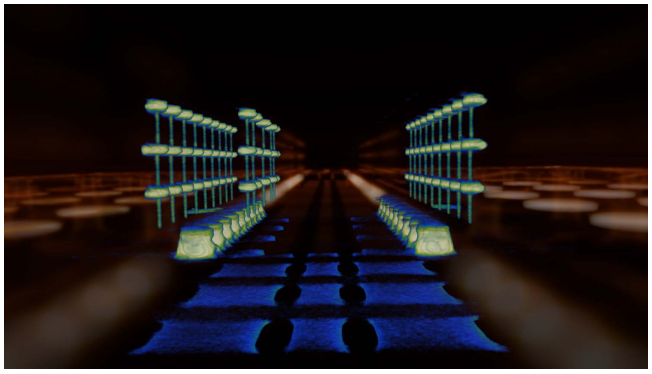

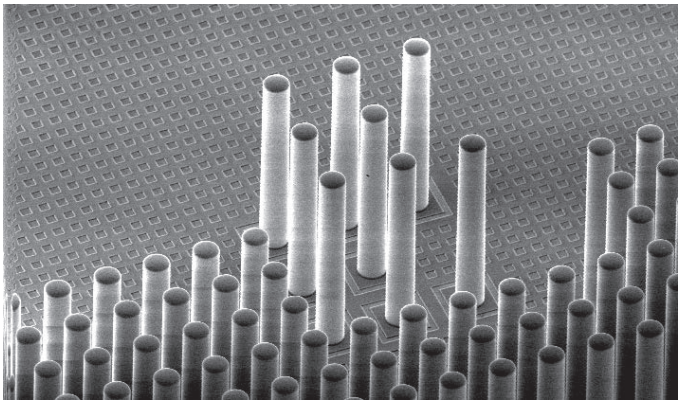

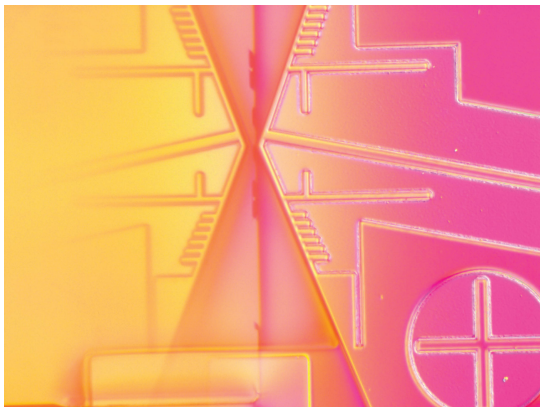

Organized by

EDFAS
Electronic Device Failure Analysis Society
ASM INTERNATIONAL

ASM INTERNATIONAL
www.asminternational.org
www.asminternational.org/istfa

Published by
ASM International®
Materials Park, Ohio 44073-0002

ISBN-13: 978-1-62708-333-1 (print)
ISBN: 978-1-62708-334-8 (pdf)

SAN: 204-7586

ASM International®
Materials Park, OH 44073-0002
www.asminternational.org

Printed in the United States of America

ISTFA™ 2020: Papers Submitted for the Planned
46th International Symposium for Testing and Failure Analysis
DOI: 10.31399/asm.cp.istfa2020p0084

Backside Integrated Circuit Magnetic Field Imaging with a Quantum Diamond Microscope

Edlyn V. Levine,[1, 2, 3, *] Matthew J. Turner,[3, 4, 5] Nicholas Langellier,[3] Thomas M. Babinec,[6] Marko Lončar,[6] and Ronald L. Walsworth[3, 4, 5]

[1]Department of Physics, Harvard University, Cambridge, MA 02138, USA
[2]The MITRE Corporation, Bedford, MA 01730, USA
[3]Quantum Technology Center, University of Maryland, College Park, MD 20742, USA
[4]Department of Physics, University of Maryland, College Park, MD 20742, USA
[5]Department of Electrical and Computer Engineering, University of Maryland, College Park, MD 20742, USA
[6]John A. Paulson School of Engineering and Applied Sciences,
Harvard University, Cambridge, Massachusetts 02138, United States
(Dated: September 18, 2020)

[*]Corresponding Author: edlynlevine@fas.harvard.edu

Abstract

We present a new method for backside integrated circuit (IC) magnetic field imaging using Quantum Diamond Microscope (QDM) nitrogen vacancy magnetometry. We demonstrate the ability to simultaneously image the functional activity of an IC thinned to 12 µm remaining silicon thickness over a wide field-of-view (3.7 x 3.7 mm^2). This 2D magnetic field mapping enables the localization of functional hot-spots on the die and affords the potential to correlate spatially delocalized transient activity during IC operation that is not possible with scanning magnetic point probes. We use Finite Element Analysis (FEA) modeling to determine the impact and magnitude of measurement artifacts that result from the specific chip package type. These computational results enable optimization of the measurements used to take empirical data yielding magnetic field images that are free of package-specific artifacts. We use machine learning to scalably classify the activity of the chip using the QDM images and demonstrate this method for a large data set containing images that are not possible to visually classify.

Introduction

We recently demonstrated simultaneous wide field-of-view, high spatial resolution, vector magnetic field imaging of static magnetic field emanations from the frontside of a wirebonded IC using a QDM [1]. We achieved approximately 10 µm resolution for all three vector magnetic field components over the 3.7 x 3.7 mm^2 field-of-view of the diamond. The present work extends the previous result to magnetic imaging of the backside of a flip chip IC with 12 µm of remaining silicon thickness (RST) to demonstrate the translatability of this method to different package types.

The QDM uses an ensemble of optically active nitrogen vacancy (NV) defects in diamond to image the magnetic fields emanated by an IC under ambient conditions. The NVs are located in a layer at the surface of a macroscopic diamond chip that is placed directly on the IC enabling 2D magnetic imaging from the entire diamond NV layer. Current densities in the IC are sources for microscopic magnetic field distributions that locally couple to the NV electron spins in the diamond. This coupling changes the NV fluorescence intensity across the diamond chip when the NVs are optically driven. The fluorescence spectra measured simultaneously across the diamond field-of-view determine the magnetic field distribution. The QDM has been used in this way to successfully image magnetic fields for a wide range of physical and biological applications [2-8].

QDM magnetic field imaging is distinctly different from scanning magnetometer point probes that leverage superconducting quantum interference devices (SQUIDs) [9-11]. The QDM measures magnetic fields simultaneously from across a large field-of-view; in contrast, a point probe needs to be scanned across an area, taking sequential measurements to generate an image. The wide field-of-view imaging capability of the QDM enables the simultaneous measurement of transient activity occurring at different locations on an IC. The magnetic sensitivity of NVs under ambient conditions enables the QDM to operate without the cryogenics necessary for SQUIDs, and is consequently inexpensive by comparison. This ambient operation also means the QDM is robust and can operate for weeks without need to calibrate or change cryogenics. NVs also afford the ability to measure all magnetic field components simultaneously, rather than only a single component as measured by SQUIDs, and has additional parameters such as resonance linewidth that can be used to extract further information about the magnetic sources.

Magnetic field imaging of ICs is a powerful diagnostic measurement for fault isolation in ICs [12]. The fields generated by IC current densities pass through most standard IC materials to yield simultaneous structural and functional information about the chip. Extracting this information from measured magnetic field data requires a detailed understanding

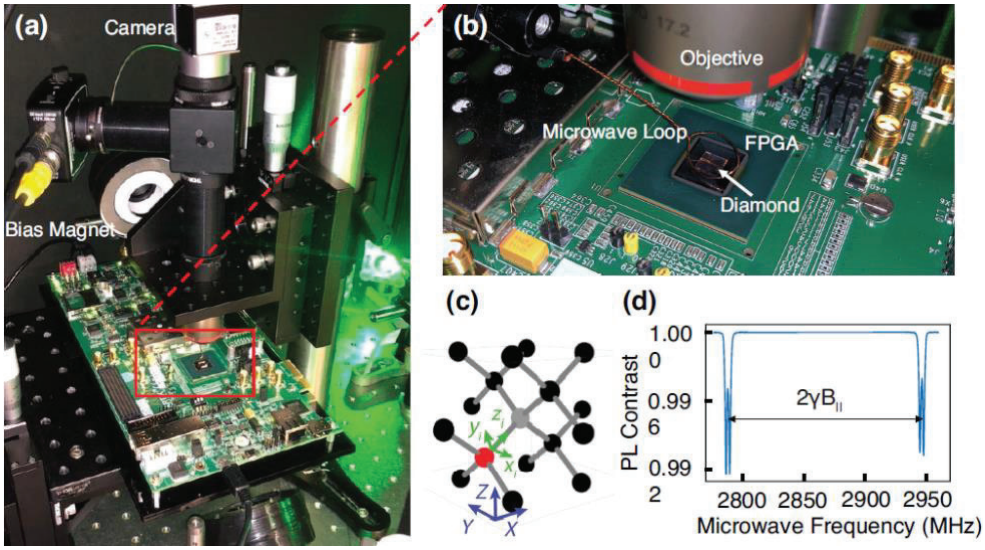

Figure 1. (a) QDM experimental setup showing the camera, bias magnets, and green light due to the laser illumination. The red box is magnified in (b) to show the objective, microwave antenna, FPGA, and the diamond chip sitting on top of the FPGA. (c) The diamond crystal lattice is shown with a single NV defect composed of a substitutional nitrogen atom (red) and a neighboring vacant lattice site (grey). (d) Data showing the optically detected magnetic resonance (ODMR) peaks due to Zeeman splitting of the ms = ±1 spin ground state for an applied bias field. Measured NV photoluminescence (PL) contrast decreases for applied microwave frequencies on resonance with the ms = 0 ⟶ ms = ±1 transitions. The difference between these resonance frequencies is proportional to $2\gamma B_{\parallel}$, where $\gamma = 2.803 \times 10^4$ MHz/T is the NV gyromagnetic ratio, and $B_{\parallel}$ is the component of the bias field parallel to the NV axis. Each resonance line is split into two peaks due to hyperfine interaction between the NV and the ^{15}N nucleus.

of the magnetic field interactions with the IC materials. In this work, we study the impacts of the flip chip package type and package materials on magnetic field imaging. We use FEA modeling to characterize the magnetic field interaction with IC materials. These modeling results also guide optimization of the measurement protocol for the flip chip package architecture under study. We use programmed variation of the activity in the IC, identical to the method used in [1], to generate complex magnetic field patterns that are imaged by the QDM and classified using machine learning techniques.

Experimental Methods

Images of the QDM setup are show in Figs. 1(a) and 1(b). The QDM consists of a pair of SmCo bias magnets applying a bias field of $B_{\parallel}$ = 28.6 G = 2.8 mT parallel to the [111] NV axis, a 7 mm diameter microwave loop antenna delivering 1 W of microwave power to the NVs, a 4x magnification, 0.13 NA objective to collect NV fluorescence over the large diamond field-of-view, a CMOS camera to measure the fluorescence, a 532 nm laser (off image) delivering 1 W continuous wave (CW) illumination over a 5 x 5 mm^2 area, and the diamond chip with NV defects such as that depicted in 1(c). This setup is identical to that used in the previous work [1] with slight modifications to accommodate the size of the device under study and adjustment of the applied bias field to align with a single NV axis direction. Two different diamond chips are used in this study: the first diamond is a 4 x 4 x 0.5 mm^3 diamond substrate with a 1.7 µm isotopically pure layer of [^{12}C] ~99.995%, [^{15}N] ~15 ppm, and [NV^-] ~2 ppm; the second diamond is a 4.7 x 4.7 x 0.5 mm^3 diamond substrate with a 40 µm isotopically pure layer of [^{12}C] ~99.995%, [^{15}N] ~15 ppm, and [NV^-] ~2 ppm.

The CW optically detected magnetic resonance (ODMR) measurement protocol for single NV axis magnetometry was used for this work [13]. This protocol, identical to that used in [1], leverages 532 nm laser illumination of the entire diamond chip to initialize the NV layer in an optically bright spin state. Beam shaping optics are used to create a rectangular laser profile that delivers equal optical power across the NV layer. The NV fluorescent photons, ranging from 637 – 800 nm, resulting from continuous optical excitation are imaged onto the CMOS camera through a 633 nm longpass filter that is used to remove 532 nm from the laser. Application of a microwave field with a frequency on resonance with the magnetic-field-dependent NV spin transition energy cause a decrease in the fluorescence intensity. The frequency of the applied microwave field is swept to obtain ODMR spectra, such as that shown in 1(d), simultaneously for each pixel of the camera image. The separation between the two resonance features, given by dips in the fluorescence contrast, is proportional to the total magnetic field experienced by the NVs contributing to a given pixel. An image of the IC's magnetic field distribution is than calculated by fitting the ODMR spectra and subtracting the applied

magnetic bias field, yielding the magnetic field contribution from the IC alone.

The Xilinx 7-series Artix FPGA (XC7A200T-2FBG676C) shown in Fig. 2(a) is selected for this study. This field programmable gate array (FPGA) has a 11 x 12 mm^2 silicon die, configured in a flip chip package. Figure 2(b) shows an x-ray image of the die and its package; an array of C4 bumps connecting the die to the package is clearly visible, and a notional outline of the diamond field-of-view is indicated. Figure 2(c) shows a scanning electron microscope (SEM) image of the FPGA's cross section clearly showing the C4 bumps connecting the silicon die to the package substrate. The die of the chip was thinned to 12 µm RST to enable small stand-off distance of magnetic field images. A magnification of the gate level is shown in Fig. 2(d). The metal stack is approximately 10 µm thick with the top metal layer farthest from the gates.

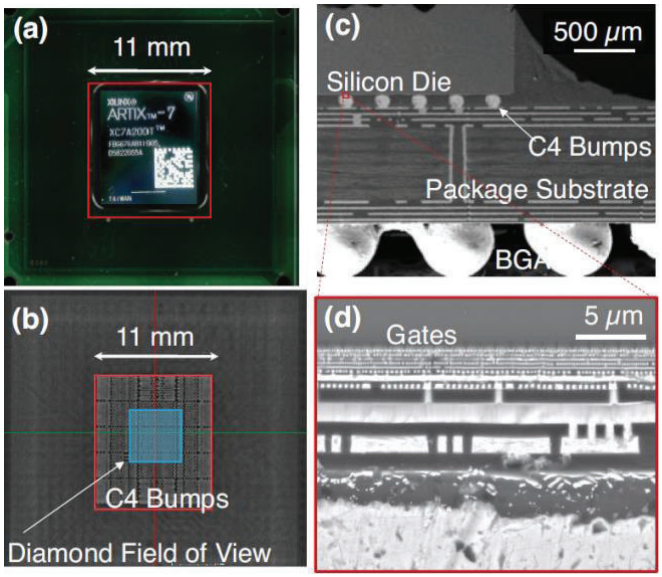

Figure 2. (a) The flip chip Xilinx Artix-7 series FPGA used in this study is shown with silicon die location indicated in red. (b) An X-ray image of the chip reveals the grid of C4 bumps connecting the die (red outline) to the package substrate. The blue box indicates the approximate location and size of the diamond chip relative to the FPGA. (c) Scanning electron microscope (SEM) image of the FPGA cross section. To enable backside access, the ~700 µm of silicon was thinned to 12 µm RST. (d) Magnified SEM image showing multiple metallization layers.

The Xilinx Artix-7 FPGA AC701 Evaluation Kit is used to configure this Artix-7 FPGA. Clusters of three-inverter ring oscillators (ROs) are implemented using the Xilinx Vivado Design Suite®. These RO clusters are of variable size and are placed at one of four specific location-locked regions on the die. The tunable size and location of the RO clusters allow for control of the magnitude and spatial distribution of current on the die, thereby allowing for the creation of distinguishable current patterns for QDM measurements. The FPGA's active states are defined by both the size and location of the ring oscillator clusters and are randomized during measurement sequences to reduce the impact of systematic noise.

Results and Analysis

A. Backside Magnetic Field Images of the Flip Chip

Figure 3 shows the magnetic field images resulting from the spatially localized RO clusters. These data were taken with the 1.7 µm NV layer diamond. The location of the diamond chip on the die is shown in Fig. 3(a) and aligned with the C4 bumps that are evident in the x-ray image. Figure 3(b) shows the location of the four RO clusters in regions labeled R1, R2, R3, and R4 within the diamond field-of-view outlined in blue. The magnetic field image measured for 200 ROs active in each of these regions is plotted in Fig. 3(c). The field pattern for each region corresponds to the expected location shown in Fig. 3(b) indicating that the relative locations of the regions in the Vivado Floorplanner correspond to the physical locations on the die.

A pattern of artifacts also appears in the magnetic field images in Fig. 3(c) having the same spatial distribution as the C4 bumps evident in the x-ray image in Fig. 3(a). The artifacts are a result of large magnetic field contributions from the C4 bumps that distort the ODMR spectra for the NVs in the neighborhood of the C4 bumps. These large magnetic field distortions cause a lack of convergence for the fitting required to extract the magnetic field information from the ODMR data. The presence of these artifacts is thus unique to the flip chip package and can be leveraged as a feature to determine the exact location of the magnetic field image with respect to the die during post-processing as shown in Fig. 3(a).

The measured magnetic fields for the flip chip are distinct from those we previously measured on the wire-bond FPGA [1]. The wirebond FPGA was similarly a Xilinx 7-series Artix FPGA (XC7A100T-1CSG3 24C) programmed with the same ring oscillator functionality. Figure 4 shows an example of the wirebond FPGA magnetic field images taken with the QDM. In the case of the wirebonded chip, we were able to achieve full vector field images due to the lack of C4 bump distortions; vector field imaging of the flip chip will ultimately be possible with improved experimental methods and data analysis. The chip was also decapsulated allowing for the diamond to be placed approximately 5 µm off the top metal layer giving rise to high resolution images of the currents flowing in the power distribution network. By contrast, the flip chip has 12 µm RST and an additional 10 µm of metallization layers separating the NV layer from the top metal layer, thus the clear traces of the power distribution network are not evident in Fig. 3(c). However, the magnetic fields from currents giving rise to the ROs are clearly discernible in Fig. 3(c) despite the larger stand-off distance, the heterogeneous magnetic background, and the large magnetic gradients from the C4 bumps introducing aberrations in the analysis.

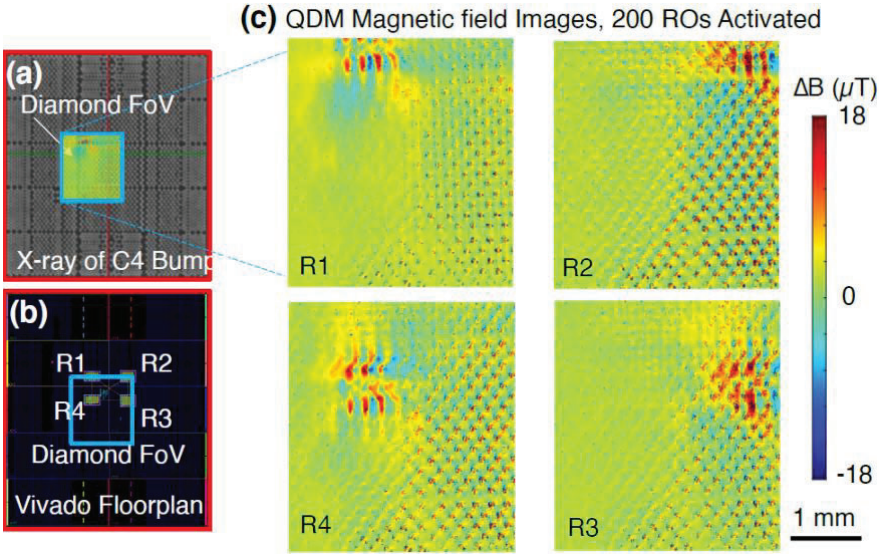

Figure 3. (a) Field-of-view of the diamond shown superimposed on the x-ray image of the FPGA. Magnetic artifacts of the C4 bumps are aligned with the x-ray imaged C4 bumps to determine the exact location of the diamond field-of-view. (b) Image of the Vivado Floorplanner showing the locations of four clusters of ROs that are placed in regions labeled R1, R2, R3, and R4 that are within the diamond field-of-view (indicated in blue). (c) Magnetic field maps are shown for 200 ring oscillators active in one of each of the four regions, R1, R2, R3, and R4, labeled in the image. These data were taken using a ^{15}N diamond with a 1.7 μm thick NV layer and a 3.5 x 3.5 mm^2 field-of-view.

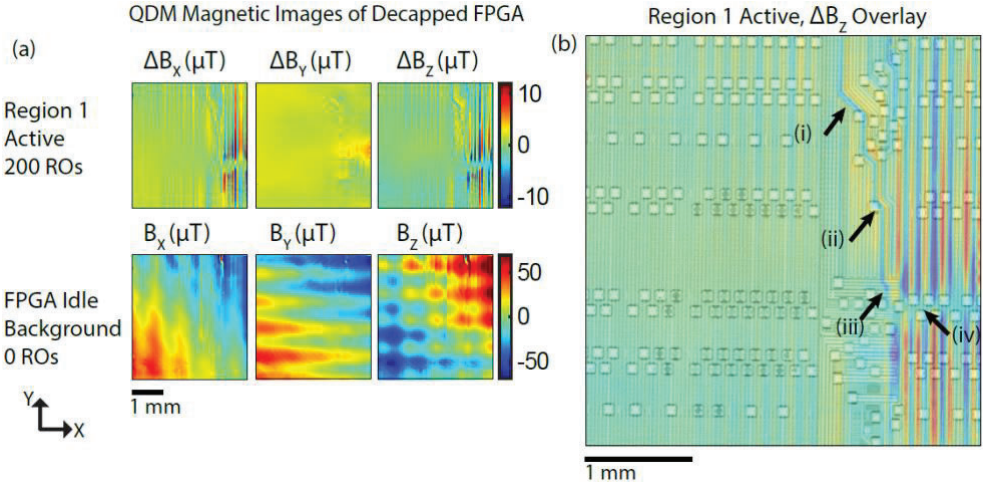

Figure 4. (a) Frontside vector magnetic field images taken of a wirebonded Artix 7 with 200 ROs active, and zero ROs studied. These data were taken with a diamond chip containing a 13 μm surface layer of NV centers. (b) The B_z data is plotted in transparency over a high-resolution optical image of circuit die. Figures (a) and (b) reprinted from [1] with permission.

The initial results of Fig. 3(c) demonstrate the first step toward backside imaging and are not representative of the limiting capability of the QDM. The pattern of systematic aberrations that appear in the data provide a means of alignment of the field-of-view with the IC and are easy to fix in postprocessing. The next few sections further demonstrate that detailed modeling of the magnetic properties of the package can yield insight into the optimization of the magnetic field measurements to improve imaging results.

B. Modeling the Impact of Magnetically Active Package Materials

Energy-dispersive X-ray spectroscopy (EDS) is used to determine the material composition of the C4 bumps. Figure 5(a) plots the results of EDS superimposed on the SEM cross sectional image. The color in each region indicates the majority

element. The C4 bump is approximately 74% tin with a layer of under bump metallization (UBM) composed of approximately 58% nickel with an additional aluminum pad connecting to the silicon die. Nickel is a ferromagnetic element that contributes to the total measured field and potentially interacts with the applied bias field, B_0. Magnetic shifts resulting from the C4 bumps are measured by the QDM with a 40 µm NV layer diamond for an idle IC with no ROs shown in Fig. 5(b).

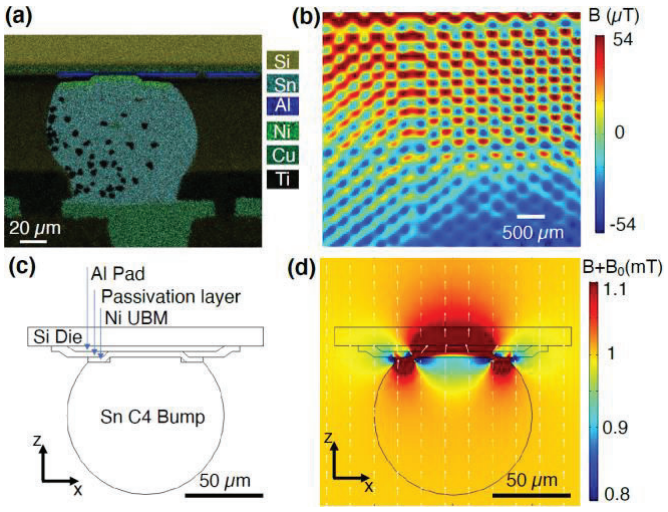

Figure 5. (a) Energy-dispersive X-ray spectroscopy (EDS) image of a single C4 bump from the SEM image in Fig. 2(c). Colors indicate the element of largest percent composition per region. (b) The measured magnetic field shifts due to the C4 bumps. These data were taken using a ^{15}N diamond with a 40 µm thick NV layer and a 4.7 x 4.7 mm^2 diamond with a 3.4 x 3.2 mm^2 field-of-view. (c) Geometry used to model the magnetic effects of a single C4 bump. (d) Simulated magnetic field resulting from a single C4 bump due to a 1 mT field applied in the z direction; white arrows indicate total magnetic field direction.

A FEA model is implemented in COMSOL Multiphysics 5.4 to calculate the contribution of the nickel UMB to the measurable magnetic field. A cross section the model geometry is shown in Fig. 5(c) consisting of the tin C4 bump, nickel UMB, aluminum pad, passivation layer, and silicon die. COMSOL's Magnetic Field (mf) module was used to solve the magnetostatic equations for different applied magnetic bias fields, B_0, assuming a relative permeability of 100 for nickel. This assumption treats nickel in a manner akin to soft iron.

A cross section of the total magnetic field resulting from this simulation with a 1 mT bias field applied in the z direction is shown in Fig. 5(d). The effective measurement plane is approximately 20 µm above the top of the 12 µm silicon layer where the total magnetic field is equal to the bias field plus the contribution from the nickel UBM layer, B_0+B, is approximately 1.05 mT. Subtraction of the 1 mT B_0_field gives $B \approx 50$ µT for the FEA model, comparing well to the approximately 50 µT measured in Fig. 5(b).

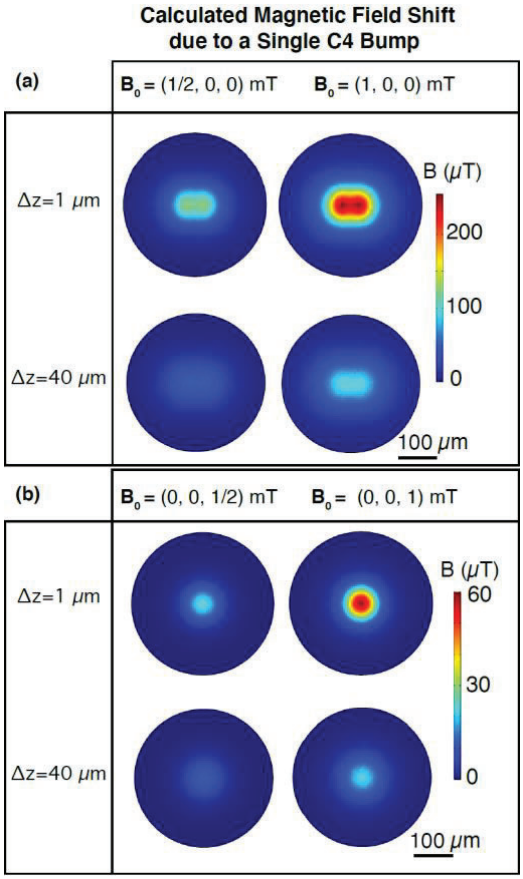

Figure 6. Calculated magnetic field in the NV measurement plane due to a single C4 bump, Fig. 5(c), for different NV layer thicknesses and different magnitudes of the magnetic bias fields applied in the (a) x direction and (b) z direction. The larger NV layer measures a weaker field due to the larger effective stand-off distance between the NVs and the C4 bump.

The resulting magnetic field shifts in the NV measurement plane due to the C4 bumps are shown in Fig. 6 for NV layer thicknesses of 1 µm and 40 µm and an applied bias field in the x and z directions. Thicker NV layers have a larger effective standoff distance since the average NV contributing to the fluorescence signal is further away. The larger standoff distances helps mitigate the impact of the strong magnetic field gradients introduced by the C4 bumps. These C4 bump magnetic contributions are dipole-like in nature and consequently fall off as $1/r^3$ where r is the distance from the magnetic field source to the measurement plane. Thus, dipole fields diminish more quickly than the magnetic fields resulting from currents, which fall off as $1/r$ or $1/r^2$ depending on the cancellation effects of neighboring wires. Consequently, larger NV layers can be used to ameliorate the artifacts of C4 bumps by lessening the near field effects of dipole contributions while still capturing the current contributions to the fields. Better fitting and better analysis will enable us to achieve higher resolution data using the thinner diamond; this will be addressed in future work. Tunable bias fields will additionally allow us to distinguish between paramagnetic and

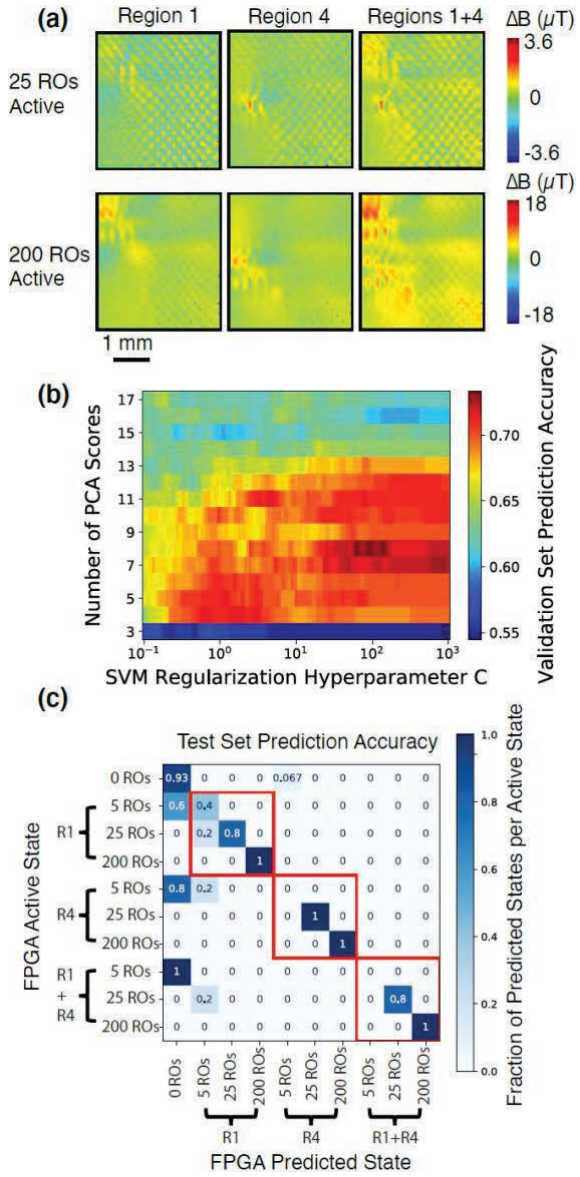

Figure 7. (a) QDM magnetic field images for different numbers of ROs active in different regions of the die. These data were taken using a ^{15}N diamond with a 40 μm thick NV layer and a 4.7 x 4.7 mm^2 diamond with a 3.4 x 3.2 mm^2 field-of-view. (b) 5-fold cross validation of the model hyperparameters. The number of PCA scores fed into the SVM classifier is varied from 3 to 17 and the SVM regularization hyperparameter is varied from 10^{-1} to 10^3. The color bar shows the average predication accuracy on the validation sets. The optimum values occur near 8 principal components and C ≈ 100. (c) Matrix of FPGA state prediction accuracies of the test set. Rows are normalized to sum to 1. Thus each row represents the distribution of predicted states for the given active state. The red boxes are states in which the active region and the predicted region are the same. We see perfect prediction accuracy for all 200 RO states and over 80% accuracy for 25 RO states. 5 RO states are often misclassified as 0 ROs. The overall state prediction accuracy is 73% for the test set.

ferromagnetic regions on the chip. This technique leverages the fact that magnetic contributions from paramagnetic field domains change with the bias field whereas ferromagnetic domains do not, and was demonstrated in previous work [14].

C. Classification of Integrated Circuit Activity

A large data set was taken to allow for machine learning classification of images. Examples of these data are shown in Fig. 7(a). Each image contains either 0, 5, 25, or 200 active ROs in either or both of two regions, labeled R1 and R4. Thus there are 4 x 3 = 12 possible FPGA operational states, where the (R1, 0 ROs), (R4, 0 ROs), and (R1+R4, 0 ROs) states are degenerate. We take 20 images of each state yielding a total data set of 240 images. Images for different numbers of ROs in different regions and multiple regions at once are shown in Fig. 7(a). These data were taken with the 40 μm NV layer diamond to minimize the effect of the magnetic gradients from the C4 bumps that were present in the 1.7 μm NV layer diamond data presented in Fig. 3(b). The diminished impact of the C4 bumps in Fig. 7(a) shows that optimization of the measurement by use of a thicker NV layer diamond succeeded in reducing the impact of the C4 bumps, consistent with the FEA analysis results.

The principal component analysis (PCA) + support vector machine (SVM) model used in [1] is used to analyze these data. The data set is separated into training and test sets using a 75%/25% split. The training set is then further split into training and validation sets using a 5-fold cross validation in order to optimize the model hyperparameters. The number of PCA scores is allowed to vary from 3 to 17 and the SVM regularization hyperparameter, C, is varied from 10^{-1} to 10^3. The resulting validation set prediction accuracy is shown in Fig. 7(b) and the optimal values occur at 8 PCA scores and C ≈ 100. A low prediction accuracy results for the first 3 PCA scores indicating that the most important principal component for state classification is the 4th principal component. The prediction accuracy drops off after about 13 PCA scores, revealing that only the first 13 principal components contain non-noise based information.

Figure 7(c) shows the results of classification are quite successful despite artifacts due to the C4 bumps. The overall state classification accuracy is 73% on the test set. States with 25 and 200 active ROs are easily classified with almost perfect accuracy, whereas states with 0 and 5 active ROs are frequently classified incorrectly. The performance of the machine learning classification will be improved in the future by including larger data sets, higher quality images (the data now is limited by experimental artifacts), and better handling of corrupted pixels (better fitting and removal). The corrupted pixels contain useful information and that will be extracted through more advanced fitting methods and leveraged for classification.

Outlook

QDM magnetic field imaging is a new method that shows promise for fault isolation applications. We have demonstrated

the ability to map magnetic fields across a wide area on an IC, and have shown how this technique translates to different package types. The present work is focused on characterizing the active states of an operating IC by leveraging magnetic field measurements. However, this magnetic imaging technique is also applicable to fault isolation methods that use probes to excite specific current pathways within an IC. Future work will explore the capability of using the QDM for isolation of specific faults such as shorts. Additionally, improvements to the analysis of ODMR data taken in proximity to the C4 bumps will enable use of diamonds with thinner NV layers leading to higher resolution magnetic field imaging. Recent results have demonstrated methods, including lock-in imaging, material improvement, and more efficient light collection that can be used to further improve performance, and increase the sensitivity and resolution of QDM measurements [15].

Acknowledgments

We thank Jim Colvin of FA Instruments for silicon thinning and many helpful discussions and insights he has given us into failure analysis. This project was fully funded by the MITRE Corporation through the MITRE Innovation Program. This work was performed in part at the Center for Nanoscale Systems (CNS), a member of the National Nanotechnology Coordinated Infrastructure Network (NNCI), which is supported by the National Science Foundation under NSF award no. 1541959. CNS is part of Harvard University.

References

[1] M. J. Turner, N. Langellier, R. Bainbridge, D. Walters, S. Meesala, T. M. Babinec, P. Kehayias, A. Yacoby, E. Hu, M. Lončar, R. L. Walsworth, and E. V. Levine, "Magnetic Field Fingerprinting of Integrated-Circuit Activity with a Quantum Diamond Microscope," *Phys. Rev. Applied* Vol. 14, No. 1 (2020) 014097. https://doi.org/10.1103/PhysRevApplied.14.014097

[2] L. M. Pham, D. Le Sage, P. L. Stanwix, T. K. Yeung, D. Glenn, A. Trifonov, P. Cappellaro, P. R. Hemmer, M. D. Lukin, H. Park, A. Yacoby, and R. L.Walsworth, "Magnetic field imaging with nitrogen-vacancy ensembles," *New Journal of Physics* Vol. 13 (2011) 045021. https://doi.org/10.1088/1367-2630/13/4/045021

[3] M. J. H. Ku, T. X. Zhou, Q. Li, Y. J. Shin, J. K. Shi, C. Burch, L. E. Anderson, A. T. Pierce, Y. Xie, A. Hamo, U. Vool, H. Zhang, F. Casola, T. Taniguchi, K. Watanabe, M. M. Fogler, P. Kim, A. Yacoby, and R. L. Walsworth, "Imaging viscous flow of the Dirac fluid in graphene," *Nature* Vol. 583 (2020) pp. 537-41. https://doi.org/10.1038/s41586-020-2507-2

[4] J. F. Barry, M. J. Turner, J. M. Schloss, D. R. Glenn, Y. Song, M. D. Lukin, H. Park, and R. L. Walsworth, "Optical magnetic detection of single-neuron action potentials using quantum defects in diamond," *Proceedings of the National Academy of Sciences* Vol. 113, No. 49 (2016) pp. 14133-8. https://doi.org/10.1073/pnas.1601513113

[5] A. Nowodzinski, M. Chipaux, L. Toraille, V. Jacques, J.-F. Roch, and T. Debuisschert, "Nitrogen-Vacancy centers in diamond for current imaging at the redistributive layer level of Integrated Circuits," *Microelectronics Reliability* Vol. 55, No. 9-10 (2015) pp. 1549-53. https://doi.org/10.1016/j.microrel.2015.06.069

[6] D. A. Simpson, J.-P. Tetienne, J. McCoey, K. Ganesan, L. T. Hall, S. Petrou, R. E. Scholten, and L. C. L. Hollenberg, "Magneto-optical imaging of thin magnetic films using spins in diamond," *Scientific Reports* Vol. 6 (2016) 22797. https://doi.org/10.1038/srep22797

[7] D. Le Sage, K. Arai, D. R. Glenn, S. J. DeVience, L. M. Pham, L. Rahn-Lee, M. D. Lukin, A. Yacoby, A. Komeili, and R. L. Walsworth, "Optical magnetic imaging of living cells," *Nature* Vol. 496 (2013) pp. 486-9. https://doi.org/10.1038/nature12072

[8] R. R. Fu, B. P. Weiss, E. A. Lima, R. J. Harrison, X.- N. Bai, S. J. Desch, D. S. Ebel, C. Suavet, H. Wang, D. Glenn, D. Le Sage, T. Kasama, R. L. Walsworth, and A. T. Kuan, "Solar nebula magnetic fields recorded in the Semarkona meteorite," *Science* Vol. 346 (2014) pp. 1089-92. https://doi.org/10.1126/science.1258022

[9] A. Orozco, J. Gaudestad, N. E. Gagliolo, C. Rowlett, E. Wong, A. Jeffers, B. Cheng, F. C. Wellstood, A. B. Cawthorne, and F. Infante, "3D Magnetic Field Imaging for Non-Destructive Fault Isolation," *Proc 39th Int'l Symp for Testing and Failure Analysis (ISTFA)*, San Jose, CA, November 2013, pp.189-93.

[10] J. Gaudestad and A. Orozco, "Magnetic Field Imaging for non destructive 3D IC testing," *Microelectronics Reliability* Vol. 54, No. 9-10 (2014) pp. 2093-8. https://doi.org/10.1016/j.microrel.2014.07.080

[11] J. Gaudestad, N. Gagliolo, V. Talanov, R. Yeh, and C. Ma, "High resolution Magnetic Current Imaging for die level short localization," *Proc 20th IEEE Int'l Symp on the Physical and Failure Analysis of Integrated Circuits (IPFA)*, Suzhou 2013, pp. 347-50. https://doi.org/10.1109/IPFA.2013.6599179

[12] A. Orozco, "Magnetic Field Imaging for Electrical Fault Isolation," *Microelectronics Failure Analysis Desk Reference*, T. Gandhi, Ed. ASM International (2019). https://doi.org/10.31399/asm.tb.mfadr7.t91110111

[13] E. V. Levine, M. J. Turner, P. Kehayias, C. A. Hart, N. Langellier, R. Trubko, D. R. Glenn, R. R. Fu, and R. L. Walsworth, "Principles and techniques of the quantum diamond microscope," *Nanophotonics* Vol. 8 (2019) 1945. https://doi.org/10.1515/nanoph-2019-0209.

[14] D. R. Glenn, R. R. Fu, P. Kehayias, D. Le Sage, E. A. Lima, B. P. Weiss, and R. L. Walsworth, "Micrometer‐scale magnetic imaging of geological samples using a quantum diamond microscope," *Geochemistry, Geophysics, Geosystems* Vol. 18, No. 8 (2017) pp 3254-67. https://doi.org/10.1002/2017GC006946

[15] M. Turner, *Quantum Diamond Microscopes for Biological Systems and Integrated Circuits*, Ph.D. thesis, Harvard University (2020)